

Nonlinear Dynamics and Regional Variations in the MJO Skeleton

ANDREW J. MAJDA

*Department of Mathematics, and Center for Atmosphere–Ocean Science, Courant Institute,
New York University, New York, New York*

SAMUEL N. STECHMANN

Department of Mathematics, University of Wisconsin—Madison, Madison, Wisconsin

(Manuscript received 10 February 2011, in final form 10 June 2011)

ABSTRACT

A minimal, nonlinear oscillator model is analyzed for the Madden–Julian oscillation (MJO) “skeleton” (i.e., its fundamental features on intraseasonal/planetary scales), which includes the following: (i) a slow eastward phase speed of roughly 5 m s^{-1} , (ii) a peculiar dispersion relation with $d\omega/dk \approx 0$, and (iii) a horizontal quadrupole vortex structure. Originally proposed in recent work by the authors, the fundamental mechanism involves neutrally stable interactions between (i) planetary-scale, lower-tropospheric moisture anomalies and (ii) the envelope of subplanetary-scale, convection/wave activity. Here, the model’s nonlinear dynamics are analyzed in a series of numerical experiments, using either a uniform sea surface temperature (SST) or a warm-pool SST. With a uniform SST, the results show significant variations in the number, strength, and/or locations of MJO events, including, for example, cases of a strong MJO event followed by a weaker MJO event, similar to the Tropical Ocean and Global Atmosphere Coupled Ocean–Atmosphere Response Experiment (TOGA COARE). With a warm-pool SST, MJO events often begin as standing oscillations and then propagate slowly eastward across the warm pool, a behavior imitating MJOs in nature. While displaying the fundamental features of the MJO skeleton, these MJO events had significant variations in their lifetimes and regional extents, and they displayed intense, irregular fluctuations in their amplitudes. The model reproduces all of these features of the MJO skeleton without including mechanisms for the MJO’s “muscle,” such as refined vertical structure and upscale convective momentum transport from subplanetary-scale convection/waves. Besides these numerical experiments, it is also shown that the nonlinear model conserves a total energy that includes a contribution from the convective activity.

1. Introduction

The Madden–Julian oscillation (MJO) is the dominant component of intraseasonal (≈ 30 – 60 days) variability in the tropics (Madden and Julian 1971, 1972, 1994). It is an equatorial wave envelope of complex multiscale convective processes, coupled with planetary-scale ($\approx 10\,000$ – $40\,000$ km) circulation anomalies. Individual MJO events often begin with a standing wave in the Indian Ocean, followed by eastward propagation across the western Pacific Ocean at a speed of roughly 5 m s^{-1} (Zhang 2005). In addition to its significance in its own right, the MJO

also significantly affects many other components of the atmosphere–ocean–earth system, such as monsoon development, intraseasonal predictability in midlatitudes, and the development of the El Niño–Southern Oscillation (ENSO; Lau and Waliser 2005; Zhang 2005).

Despite the widespread importance of the MJO, present-day computer general circulation models (GCMs) typically have poor representations of it (Lin et al. 2006; Kim et al. 2009). Moreover, simple theories for the MJO have also been largely unsuccessful, both in explaining the MJO’s fundamental mechanisms and in reproducing all of its fundamental features together. There have been a large number of theories attempting to explain the MJO through mechanisms such as evaporation–wind feedback (Emanuel 1987; Neelin et al. 1987), boundary layer frictional convergence instability (Wang and Rui 1990), stochastic linearized convection (Salby et al. 1994),

Corresponding author address: Samuel N. Stechmann, Department of Mathematics, University of Wisconsin—Madison, 480 Lincoln Dr., Madison, WI 53706.
E-mail: stechmann@wisc.edu

radiation instability (Raymond 2001), and the planetary-scale linear response to moving heat sources (Chao 1987). These theories are all at odds with the observational record in various crucial ways (Lau and Waliser 2005; Zhang 2005), and it is therefore likely that none of them captures the fundamental physical mechanisms of the MJO. Nevertheless, they all provide some insight into the mechanisms of the MJO.

Besides traditional GCMs and simple theories, further insight on the MJO has also been gained through other theoretical and modeling studies. For instance, insight has been gained from the study of MJO-like waves in multi-cloud model simulations (Khouider and Majda 2007; Majda et al. 2007; Khouider and Majda 2008b; Khouider et al. 2011) and in superparameterization computer simulations (Grabowski 2001, 2003; Grabowski and Moncrieff 2004; Moncrieff 2004; Benedict and Randall 2009; Thayer-Calder and Randall 2009), which appear to capture many of the observed features of the MJO by accounting for smaller-scale convective structures within the MJO envelope. As another example, convective momentum transport from subplanetary-scale waves/convection appears to play a role in producing some features of the MJO's planetary-scale envelope, as shown in multiscale asymptotic models (Majda and Biello 2004; Biello and Majda 2005; Biello and Majda 2006; Biello et al. 2007; Majda and Stechmann 2009a). Despite all of the interesting contributions listed above—from GCMs, simplified models, and everything in between—no theory for the MJO has yet been generally accepted, and the problem of explaining the MJO has been called the search for the Holy Grail of tropical atmospheric dynamics (Raymond 2001). Building on earlier work, the present paper contributes to this search.

While theory and simulation of the MJO remain difficult challenges, they are guided by the generally accepted, fundamental features of the MJO on intraseasonal–planetary scales. These features are referred to here as the MJO's "skeleton" (Majda and Stechmann 2009b), and they have been identified relatively clearly in observations:

- 1) A slow eastward phase speed of roughly 5 m s^{-1} (Hendon and Salby 1994; Hendon and Liebmann 1994; Maloney and Hartmann 1998; Kiladis et al. 2005),
- 2) A peculiar dispersion relation with $d\omega/dk \approx 0$ (Salby and Hendon 1994; Wheeler and Kiladis 1999; Roundy and Frank 2004), and
- 3) A horizontal quadrupole vortex structure (Hendon and Salby 1994; Hendon and Liebmann 1994; Maloney and Hartmann 1998).

While these are the salient planetary–intraseasonal features of MJO composites, individual MJO events often

have additional features, such as westerly wind bursts (Lin and Johnson 1996; Majda and Biello 2004; Biello and Majda 2005; Majda and Stechmann 2009a), complex vertical structures (Lin and Johnson 1996; Myers and Waliser 2003; Kikuchi and Takayabu 2004; Kiladis et al. 2005; Tian et al. 2006), and complex convective features within the MJO envelope (Nakazawa 1988; Hendon and Liebmann 1994; Dunkerton and Crum 1995; Yanai et al. 2000; Houze et al. 2000; Masunaga et al. 2006; Kiladis et al. 2009). Since these additional features add detailed character to each MJO's structure, and since these features often account for additional strength beyond the MJO's skeleton, they are referred to here as the MJO's "muscle" (Majda and Stechmann 2009b).

Recently, Majda and Stechmann (2009b) introduced a minimal dynamical model that captures the MJO's intraseasonal/planetary-scale features 1–3, together, for the first time in a simple model. The model is a nonlinear oscillator model for the MJO skeleton and the skeleton of tropical intraseasonal variability in general. The fundamental mechanism of the model involves interactions between (i) planetary-scale, lower-tropospheric moisture anomalies and (ii) subplanetary-scale, convection/wave activity (or, more precisely, the planetary-scale envelope of the subplanetary-scale convective activity).

While the linear waves of the skeleton model were analyzed in Majda and Stechmann (2009b), the purpose of the present paper is to study the model's nonlinear dynamics. Do the nonlinear dynamics also reproduce a realistic MJO skeleton? In what ways do the linear waves interact nonlinearly? In what ways do the waves interact nonlinearly with a regionally varying base state, which represents the western Pacific warm pool? When the warm pool is present, does the MJO skeleton often begin as a standing wave and then propagate slowly eastward? These questions and others are the focus of this paper.

The paper is organized as follows. In section 2, the model, its energetics, and its linear waves are described. Next, nonlinear numerical solutions are presented with a uniform base state [i.e., sea surface temperature (SST)] (section 3) and with a regionally varying, warm-pool SST (section 4). Finally, section 5 presents the conclusions.

2. Model description, energetics, and linear theory

a. Model description

The MJO skeleton model was originally proposed and developed by Majda and Stechmann (2009b). It is a nonlinear oscillator model for the MJO skeleton as a neutrally stable wave (i.e., the model includes neither damping nor instability mechanisms). The fundamental mechanism of the oscillation involves interactions

between (i) planetary-scale, lower-tropospheric moisture anomalies and (ii) subplanetary-scale, convection/wave activity (or, more precisely, the planetary-scale envelope of the subplanetary-scale convective activity). These quantities are represented by the variables q and a :

- q : Lower-tropospheric moisture anomaly.
- a : Amplitude of the convection/wave activity envelope.

It is noteworthy that, for the MJO skeleton model, it is only the amplitude of the convection/wave activity envelope that is needed, not any of the details of the particular convection/waves that make up the envelope (Nakazawa 1988; Hendon and Liebmann 1994; Yanai et al. 2000; Houze et al. 2000; Masunaga et al. 2006; Kiladis et al. 2009), although the specific details can be important for convective momentum transports or other features of the MJO’s muscle.

A key part of the q – a interaction is how the moisture anomalies influence the convection. The premise is that, for convective activity on planetary/intraseasonal scales, it is the time tendency of convective activity—not the convective activity itself—that is most directly related to the (lower tropospheric) moisture anomaly. In other words, rather than a functional relationship $a = a(q)$, it is posited that q mainly influences the tendency (i.e., the growth and decay rates) of the convective activity. The simplest equation that embodies this idea is

$$a_t = \Gamma qa, \tag{1}$$

where Γ is a constant of proportionality: positive (negative) low-level moisture anomalies create a tendency to enhance (decrease) the envelope of convection/wave activity.

The basis for (1), and the physics behind it, comes from a combination of observations, modeling, and theory. Generally speaking, it is well-known that tropospheric moisture content plays a key role in regulating convection (Austin 1948; Malkus 1954; Brown and Zhang 1997; Tompkins 2001; Derbyshire et al. 2004; Grabowski and Moncrieff 2004; Holloway and Neelin 2009; Waite and Khouider 2010). In observations, specifically on planetary/intraseasonal scales, several studies have shown that the lower troposphere tends to moisten during the suppressed convection phase of the MJO, and lower-tropospheric moisture leads the MJO’s heating anomaly (Myers and Waliser 2003; Kikuchi and Takayabu 2004; Kiladis et al. 2005; Tian et al. 2006), which suggests the relationship in (1). Furthermore, this relationship is also suggested by simplified models for synoptic-scale convectively coupled waves (Khouider and Majda 2006; Khouider and Majda 2008a; Majda and

TABLE 1. Model parameters. The additional parameter \bar{H} is arbitrary, and its value was chosen to be 10 K day^{-1} .

Parameter	Value	Description
\bar{Q}	0.9	Background moisture stratification
Γ	1.66	Sensitivity of convective activity tendency to q anomalies
\bar{S}^{θ}	1 K day^{-1}	Radiative cooling rate

Stechmann 2009a; Stechmann et al. 2011, manuscript submitted to *Theor. Comput. Fluid Dyn.*, hereafter SMS). These models show that the growth rates of the convectively coupled waves depend on the wave’s environment, such as the environmental moisture content; and SMS estimate the value of Γ from these growth rate variations. Last, amplitude equations such as in (1) have been used in other areas of science and engineering, and they can sometimes be derived from the governing equations using systematic asymptotics [see Bourlioux and Majda (1995) and references therein]. In the atmospheric sciences, SMS show that amplitude equations can be used as a simple model for convectively coupled wave–mean flow interactions (Majda and Stechmann 2009a).

By combining the parameterization in (1) with the (long-wave scaled) linearized primitive equations, the skeleton model of Majda and Stechmann (2009b) is obtained:

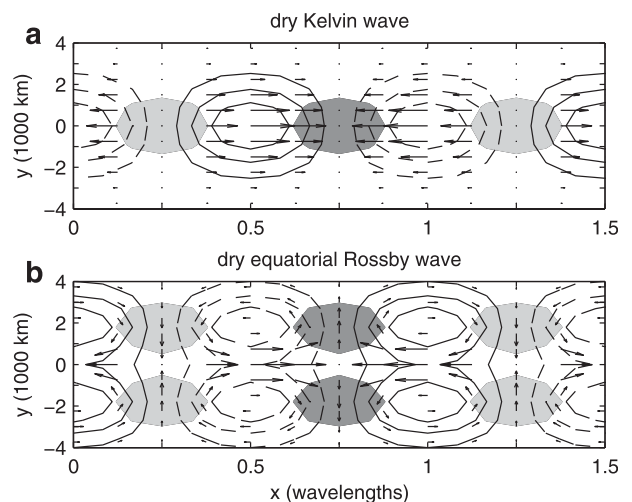


FIG. 1. Physical structures of (a) the unforced “dry” Kelvin wave and (b) the equatorial Rossby wave. Contours show lower-tropospheric pressure with positive (negative) anomalies denoted by solid (dashed) lines. The contour interval is one-fourth the maximum amplitude of the anomaly, and the zero contour is not shown. Anomalies of convergence (divergence) that are greater than two-thirds the maximum amplitude are shaded dark (light) gray.

$$\begin{aligned}
u_t - yv &= -p_x \\
yu &= -p_y \\
0 &= -p_z + \theta \\
u_x + v_y + w_z &= 0 \\
\theta_t + w &= \overline{H}a - s^\theta \\
q_t - \tilde{Q}w &= -\overline{H}a + s^q \\
a_t &= \Gamma qa.
\end{aligned} \tag{2}$$

Here u , v , and w are the zonal, meridional, and vertical velocity anomalies, respectively; p and θ are the pressure and potential temperature anomalies, respectively; and s^θ and s^q are sources of cooling and moistening, respectively. The convective heating and drying are taken to be proportional to the envelope of convection/wave activity $\overline{H}a$. Equatorial long-wave scaling has been used (Majda 2003), and the equations have been nondimensionalized in standard fashion (Majda and Stechmann 2009a).

Notice that this model contains a minimal number of parameters, summarized in Table 1: $\tilde{Q} = 0.9$, the (nondimensional) mean background vertical moisture gradient; and $\Gamma = 1.66$, or $\Gamma \approx 0.3 \text{ K}^{-1} \text{ day}^{-1}$ in dimensional units. These will be the parameter values used throughout the paper. The source terms s^θ and s^q must also be specified (see below). Also notice that the parameter \overline{H} is actually irrelevant to the dynamics (as can be seen by rescaling a); it is written here for clarity of presentation: dimensionally, it gives $\overline{H}a$ the units of a heating rate while keeping a nondimensional. The dimensional value of \overline{H} was chosen to be 10 K day^{-1} so that a typical value of a is ≈ 0.1 , similar to the nondimensional value of u .

To obtain the simplest model for the MJO, truncated vertical and meridional structures are used. For the vertical truncation, only the first baroclinic mode is used so that $u(x, y, z, t) = u(x, y, t)\sqrt{2}\cos(z)$, etc., with a slight abuse of notation. The resulting equations resemble a time-dependent version of a Matsuno–Gill model (Matsuno 1966; Gill 1980), without damping, plus equations for q and a :

$$\begin{aligned}
u_t - yv - \theta_x &= 0 \\
yu - \theta_y &= 0 \\
\theta_t - u_x - v_y &= \overline{H}a - s^\theta \\
q_t + \tilde{Q}(u_x + v_y) &= -\overline{H}a + s^q \\
a_t &= \Gamma qa.
\end{aligned} \tag{3}$$

Next, for the meridional truncation, it is assumed that a , the envelope of convection/wave activity, has a simple equatorial meridional structure proportional to

$\exp(-y^2/2)$: $a(x, y, t) = [\overline{A}(x) + A(x, t)]\pi^{-1/4}\exp(-y^2/2)$, where $\overline{A}(x)$ is a background state. For the long-wave-scaled equations, such a meridional heating structure is known to excite only Kelvin waves and the first symmetric equatorial Rossby waves (Majda 2003; Biello and Majda 2006), and the resulting meridionally truncated equations can be written as

$$\begin{aligned}
K_t + K_x &= -\frac{1}{\sqrt{2}}\overline{H}A \\
R_t - \frac{1}{3}R_x &= -\frac{2\sqrt{2}}{3}\overline{H}A \\
Q_t + \frac{1}{\sqrt{2}}\tilde{Q}K_x - \frac{1}{6\sqrt{2}}\tilde{Q}R_x &= \left(-1 + \frac{1}{6}\tilde{Q}\right)\overline{H}A \\
A_t &= \Gamma Q(\overline{A} + A),
\end{aligned} \tag{4}$$

where K and R are the amplitudes of the Kelvin and equatorial Rossby structures, respectively, as shown in Fig. 1.

An important point is that $K(x, t)$ and $R(x, t)$ are the amplitudes of the structures of Kelvin and Rossby waves, but these amplitudes in (4) need not always propagate like “dry” waves. In the absence of forcing in (4), the dry long-wave Kelvin and equatorial Rossby wave solutions are dispersionless waves that propagate at 50 and 17 m s^{-1} , respectively (Majda 2003; Biello and Majda 2006). However, in the presence of the coupled dynamical forcing A in (4), the Kelvin and equatorial Rossby wave structures can be coupled to each other and to Q and A ; and these coupled modes/structures can have propagation speeds very different from 50 or 17 m s^{-1} , and they can be dispersive. One such mode has the structure and dispersion characteristics of the MJO, as shown by Majda and Stechmann (2009b) and summarized below.

The variables u , v , θ are recovered by using the following formulas (Majda 2003; Biello and Majda 2006):

$$\begin{aligned}
u(x, y) &= \frac{1}{\sqrt{2}}\left[K(x) - \frac{1}{2}R(x)\right]\phi_0(y) + \frac{1}{4}R(x)\phi_2(y) \\
v(x, y) &= \left[\frac{1}{3}\partial_x R(x) - \frac{1}{3\sqrt{2}}\overline{H}A(x)\right]\phi_1(y), \\
\theta(x, y) &= -\frac{1}{\sqrt{2}}\left[K(x) + \frac{1}{2}R(x)\right]\phi_0(y) - \frac{1}{4}R(x)\phi_2(y)
\end{aligned} \tag{5}$$

where $\phi_0(y) = \pi^{-1/4}\exp(-y^2/2)$, $\phi_1(y) = \pi^{-1/4}\sqrt{2}y\exp(-y^2/2)$, and $\phi_2(y) = \pi^{-1/4}2^{-1/2}(2y^2 - 1)\exp(-y^2/2)$ are parabolic cylinder functions (Majda 2003; Biello and Majda 2006). The meridional structures of q and the source terms are given by $q(x, y, t) = Q(x, t)\phi_0(y)$, $s^\theta(x, y) = S^\theta(x)\phi_0(y)$, and $s^q(x, y) = S^q(x)\phi_0(y)$. In the simplest

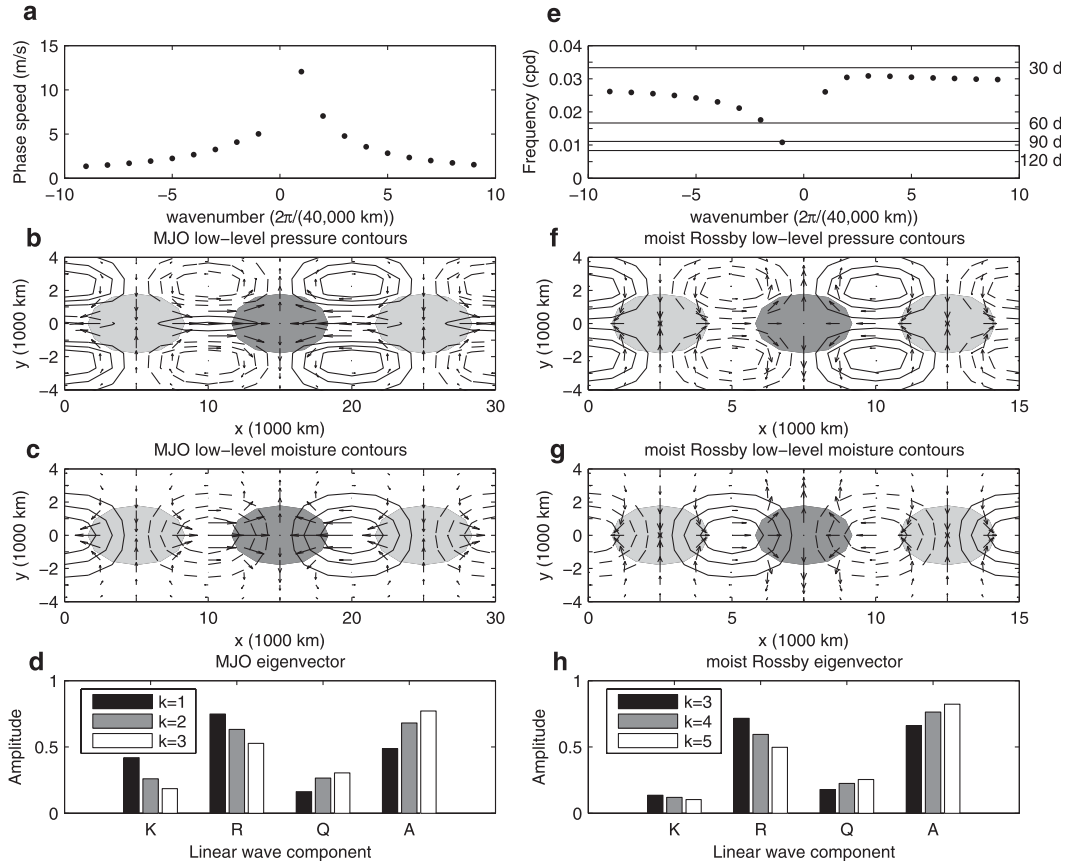


FIG. 2. Summary of low-frequency linear waves of the skeleton model in (4). (a) Phase speed ω/k as a function of wavenumber k . Eastward (westward) propagation is denoted by positive (negative) wavenumber k . (b) Horizontal structure of the $k = 2$ MJO mode. Lower-tropospheric velocity vectors are shown with contours of lower-tropospheric pressure anomalies with positive (negative) anomalies denoted by solid (dashed) lines. The contour interval is one-fourth the maximum amplitude of the anomaly, and the zero contour is not shown. (c) As in (b), but for contours of lower-tropospheric moisture anomalies. (d) Component amplitudes of the MJO eigenvector for wavenumbers $k = 1, 2$, and 3 . (e) As in (a), but for oscillation frequency $\omega(k)$. Horizontal lines denote oscillation periods of 30, 60, 90, and 120 days. (f) As in (b), but for the $k = 4$ moist Rossby mode. (g) As in (c), but for the $k = 4$ moist Rossby mode. (h) As in (d), but for the $k = 3, 4$, and 5 moist Rossby modes.

case, $S^\theta = \bar{S}^\theta = 1 \text{ K day}^{-1}$ is the uniform radiative cooling rate. Also notice that $A(x, t)$ is an anomaly from a base state $\bar{A}(x)$, which is chosen to balance the sources of cooling and moistening: $\overline{HA}(x) = S^\theta(x) = S^q(x)$. In this fashion, $\bar{A}(x)$ represents base-state variations in the simplest way, and $\bar{A}(x)$ will be used to represent the SST, as either a uniform SST (section 3) or a warm-pool SST (section 4).

b. Energetics

The nonlinear MJO skeleton model has two important energy principles, in the absence of source terms s^θ and s^q . First, the model in (3) conserves a vertically integrated moist static energy:

$$\partial_t(\theta + q) - (1 - \tilde{Q})(u_x + v_y) = 0. \tag{6}$$

Second, the model in (3) conserves a positive total energy that includes a contribution from the convective activity a :

$$\begin{aligned} \partial_t \left[\frac{1}{2} u^2 + \frac{1}{2} \theta^2 + \frac{1}{2} \frac{\tilde{Q}}{1 - \tilde{Q}} \left(\theta + \frac{q}{\tilde{Q}} \right)^2 + \frac{\bar{H}}{\Gamma \tilde{Q}} a \right] \\ - \partial_x(u\theta) - \partial_y(v\theta) = 0. \end{aligned} \tag{7}$$

TABLE 2. Summary of numerical experiments.

Case name	Base-state SST	Initial waves	Figure No.
U2	Uniform	MJO, $k = 2$	3
U12	Uniform	MJO, $k = 1$ and 2	4
U13	Uniform	MJO, $k = 1$ and 3	5
WP-MJO	Warm pool	MJO, $k = 2$	7, 8, 9, 10
WP-K	Warm pool	Kelvin, $k = 2$	11
WP-MR	Warm pool	Moist Rossby, $k = 2$	No figure

This total energy is a sum of four terms: dry kinetic energy $u^2/2$, dry potential energy $\theta^2/2$, a moist potential energy proportional to $(\theta + \bar{Q}^{-1}q)^2$ [cf. Frierson et al. (2004)], and a convective energy $\overline{H}a/(\Gamma\bar{Q})$. Note that the natural requirement on the background moisture gradient, $0 < \bar{Q} < 1$, is needed to guarantee a positive energy.

c. Linear theory

Before presenting the nonlinear dynamics of the MJO skeleton model, its linear waves are reviewed [see Majda and Stechmann (2009b) for further linear theory results]. Figure 2 summarizes the linear waves. The MJO mode captures all of the fundamental features 1–3 of the MJO skeleton: a slow eastward phase speed of $\approx 5 \text{ m s}^{-1}$ (Fig. 2a), an oscillation frequency that is roughly constant (Fig. 2e), and a horizontal quadrupole vortex structure (Fig. 2b). Furthermore, the nearly constant oscillation frequency is given by the following simple formula (Majda and Stechmann 2009b):

$$\omega \approx \sqrt{\Gamma S^{\bar{\theta}}(1 - \bar{Q})}. \quad (8)$$

On the other hand, the westward-propagating moist Rossby mode has a very low frequency that is essentially seasonal, not intraseasonal, for $k = 1$. Previously, the $k = 1$ and 2 moist Rossby modes were shown to have much smaller components of moisture Q and convective activity A in comparison to the MJO mode (Majda and Stechmann 2009b).

Here, in Fig. 2, emphasis is instead given to the $k = 3, 4$, and 5 moist Rossby modes because observational analyses often show a spectral peak at these wavenumbers and at intraseasonal frequencies (periods of greater than roughly 25 days; Wheeler and Kiladis 1999; Roundy and Frank 2004; Kiladis et al. 2009). The observed peak appears within a broader spectral band, which includes higher frequencies and greater wavenumbers, and that is associated with convectively coupled equatorial Rossby waves. It is possible that some aspects of the low-frequency Rossby wave activity are represented in the present model, although a detailed comparison of this is not the focus here. With this in mind, the model's westward-propagating low-frequency mode is referred to here as the moist Rossby mode or wave, for simplicity. In addition to the two low-frequency modes of the model shown in Fig. 2, two high-frequency modes are also present; they resemble the dry Kelvin and Rossby waves and have little contribution from moisture or convective activity.

While the model in (2)–(4) adds little complexity beyond the dry primitive equations, one might suspect that the MJO skeleton could be captured by an even simpler version of (2)–(4). In light of this, a simpler version is

briefly described now, including its strengths and limitations. To create a simpler version, the dry dynamics in (2)–(4) could be replaced by weak-temperature-gradient dynamics (Sobel et al. 2001; Majda and Klein 2003). A nice result of this approximation is that the oscillation frequency of the low-frequency waves is given exactly by (8) (see the appendix for details). However, it is not clear that this weak-temperature-gradient approximation is valid on intraseasonal/planetary scales (Majda and Klein 2003), and, more importantly, the dynamics loses its east–west asymmetry (i.e., both the eastward- and westward-propagating low-frequency modes have the same oscillation frequencies, in contrast to the results in Fig. 2).

d. Numerical methods for the nonlinear model

The remainder of the paper describes nonlinear numerical solutions of the MJO skeleton model. The numerical method used to solve (4) is a splitting method that is designed to minimize numerical dissipation. In the first step, the linear equations for K , R , and Q are solved with the linearized part of the A equation: $A_t = \Gamma Q \bar{A}$. In the second step, K , R , and Q are held fixed, and the nonlinear part of the A equation is evolved as a linear ordinary differential equation: $A_t = \Gamma Q A$. Each step is individually solved exactly: the first step using Fourier series, and the second step using the exact exponential solution (assuming Q is held fixed). The initial condition for each case is either a single linear mode or a linear combination of two linear modes, as described below and summarized in Table 2. The initial amplitude is ≈ 0.1 in nondimensional units, which corresponds to a convective heating anomaly $\overline{H}A$ of $\approx \pm 0.8 \text{ K day}^{-1}$ and a zonal wind anomaly of $\approx \pm 4 \text{ m s}^{-1}$. Note that this is nearly the largest possible amplitude for a sinusoidal anomaly because $\overline{H}(A + A)$ is always positive and $\overline{H}\bar{A} = 1 \text{ K day}^{-1}$. The spatial grid has 64 zonal grid points over the 40 000-km circumference of the earth, which yields a grid spacing of $\Delta x = 625 \text{ km}$. This grid spacing allows each planetary wavenumber 1 to ≈ 6 to be resolved by at least 10 grid points. The time step was chosen to be $\Delta t = 0.5\Delta x$ in nondimensional units, or $\Delta t \approx 1.7 \text{ h}$. The data snapshots were output twice daily. A key feature of this model is that it is very inexpensive computationally: 1600 days of simulation time takes only $\approx 20 \text{ s}$ of computer time on a typical laptop computer.

3. Nonlinear dynamics

In this section, nonlinear numerical solutions are presented with a uniform SST, as represented by the uniform base-state balance $\overline{H}A = \overline{S}^{\bar{\theta}} = 1 \text{ K day}^{-1}$. The cases are summarized in Table 2.

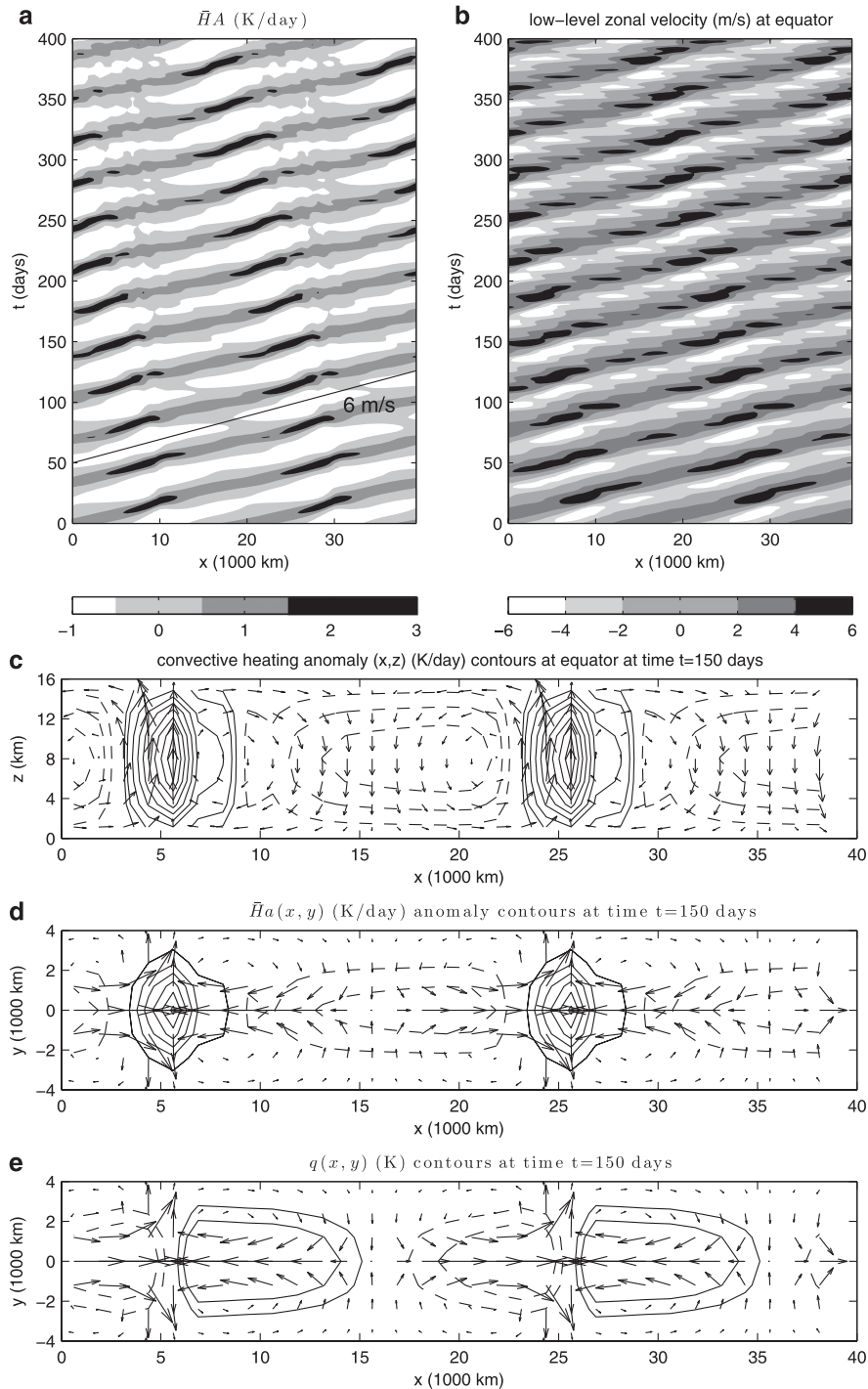


FIG. 3. Case U2: Initial wavenumber-2 MJO. (a) Contours of the amplitude of the convective activity envelope $\bar{H}A(x,t)$. (b) Contours of the low-level zonal velocity at the equator, as a function of zonal location x and time t . (c) Snapshot of zonal-vertical structure above the equator at time $t = 150$ days. Zonal and vertical velocity vectors are shown with contours of convective heating. (d) Snapshot of zonal-meridional structure at time $t = 150$ days. Low-level zonal and meridional velocity vectors are shown with contours of the amplitude of the convective activity envelope $\bar{H}a(x,y)$. (e) As in (d), but for contours of lower-tropospheric moisture $q(x,y)$. All positive (negative) contours are shown by solid (dashed) lines. For convective heating (moisture), positive contour interval is 0.3 K day^{-1} (K), negative contour interval is 0.15 K day^{-1} (K), the zero contour is not shown, and an additional positive contour is drawn at 0.15 K day^{-1} (K). Maximum zonal, meridional, and vertical velocities are 5, 3, and 0.02 m s^{-1} , respectively.

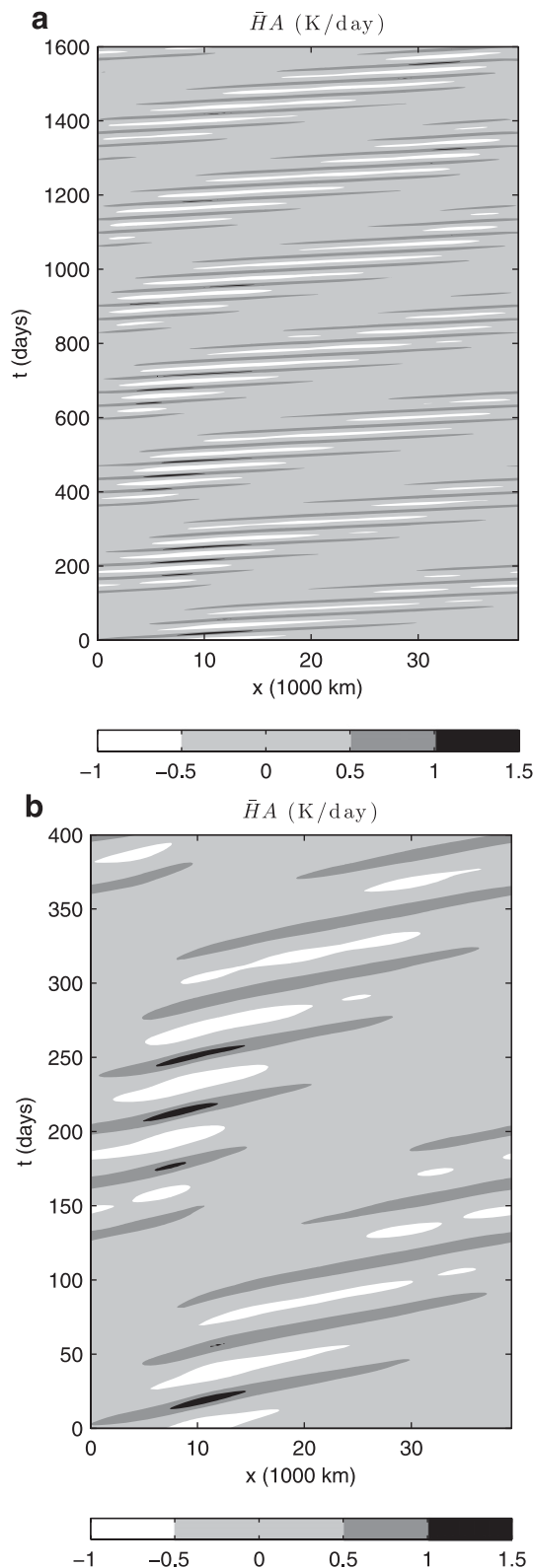


FIG. 4. Case U12: Initial wavenumbers-1 and -2 MJO. Contours show $\bar{H}A(x, t)$, the amplitude of convective activity for (a) times $t = 0$ –1600 days and (b) times $t = 0$ –400 days.

a. Case U2: Initial wavenumber-2 MJO

The simplest case is case U2 with uniform SST and an initial wavenumber-2 MJO mode. The results are shown in Fig. 3. The broad evolution is shown by the evolution of the convective activity $\bar{H}A(x, t)$ in Fig. 3a. The MJO propagates slowly eastward at roughly 6 m s^{-1} , with prominent phases of both active and suppressed convection. In this nonlinear case, the convective anomalies are asymmetric: the positive anomalies have strong fluctuations of ≈ 1 – 3 K day^{-1} , whereas the negative anomalies never fall below -1 K day^{-1} because $\bar{H}(\bar{A} + A)$ is always a positive quantity and $\bar{H}\bar{A} = 1 \text{ K day}^{-1}$. Further indication of nonlinear effects can be seen in the excitation of other types of waves: a slow, westward-propagating envelope of maximum convective activity can be seen in Fig. 3a, and fast, westward-propagating signals can be seen throughout Fig. 3b.

Snapshots of the zonal–vertical structure (Fig. 3c) and zonal–meridional structure (Figs. 3d,e) are shown at time $t = 150$ days. Two strong convective events are present at this time with each collocated with upward vertical motion and horizontal convergence of the zonal wind. Straddling the equator, a pair of anticyclones leads and a pair of cyclones trails the convective activity. Also, the maximum lower-tropospheric moisture leads the convective maximum. Hence, the nonlinear model reproduces the fundamental features of the MJO skeleton.

While the model captures the broad fundamental features of the MJO, some finer details of the MJO’s muscle are not included in this model. These details include, for instance, a refined vertical structure (Lin and Johnson 1996; Myers and Waliser 2003; Kikuchi and Takayabu 2004; Kiladis et al. 2005; Tian et al. 2006), upscale momentum transport from mesoscale convective systems and synoptic-scale convectively coupled equatorial waves (Moncrieff and Klinker 1997; Houze et al. 2000; Tung and Yanai 2002a,b; Majda and Biello 2004; Biello and Majda 2005; Majda and Stechmann 2009a), and the effect of variations in land–sea contrasts and surface fluxes (Sobel et al. 2008, 2010). These effects should amplify features such as the westerly wind burst, and they would also likely rectify some of the finer details of the phase relationships among different variables (although some phase relationships are somewhat rectified in the warm-pool case of section 4a).

b. Case U12: Initial wavenumbers-1 and -2 MJO

Case U12 illustrates the nonlinear interaction of different MJO wavenumbers, using an initial condition that is the sum of wavenumber-1 and -2 MJO modes. Figure 4a shows the broad evolution of the convective activity for 1600 days. The MJO events are organized by a slow,

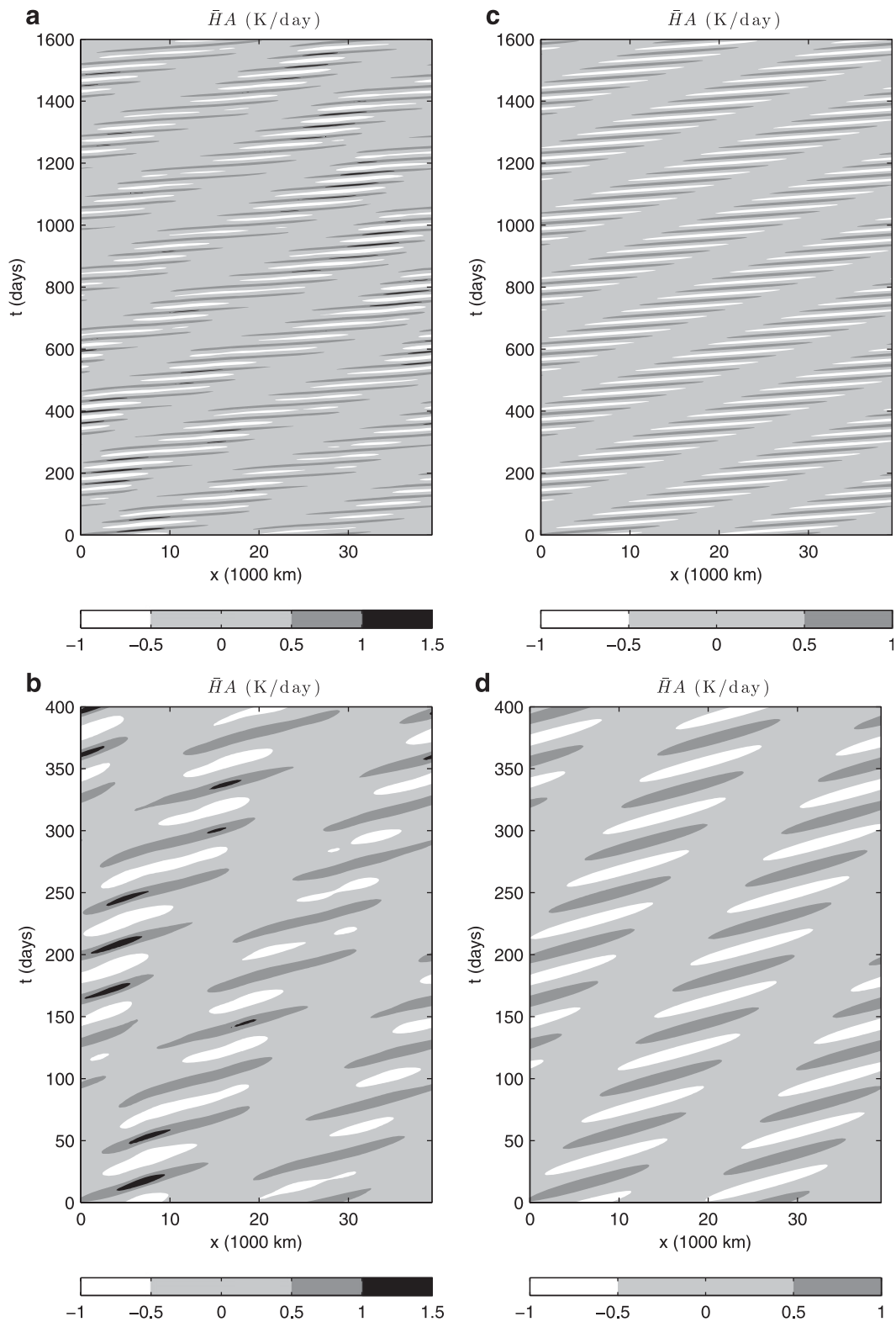


FIG. 5. Case U13: Initial wavenumbers-1 and -3 MJO. (a),(b) As in Fig. 4, but for case U13. (c),(d) As in (a),(b), but for the linear model.

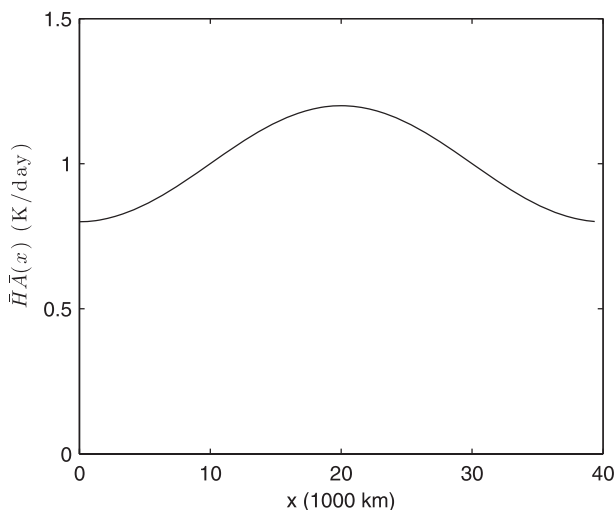


FIG. 6. Warm-pool base-state SST used for cases WP-MJO, WP-K, and WP-MR, as summarized in Table 2.

wavenumber-1, eastward-propagating envelope, whose existence is due to linear, not nonlinear, dynamics. Within this envelope, however, the individual MJO events have a variety of amplitudes and other nonlinear features that distinguish this case from purely linear dynamics. For instance, in this model simulation, it is common to see a strong MJO event followed by a weaker event (or vice versa), as was seen during the Tropical Ocean and Global Atmosphere Coupled Ocean–Atmosphere Response Experiment (TOGA COARE; Lin and Johnson 1996; Yanai et al. 2000). This is shown in greater detail in Fig. 4b; for example, near $x \approx 10\,000$ km, strong events at roughly $t = 20$ and 250 days are followed by weaker events at roughly $t = 50$ and 290 days, respectively.

c. Case U13: Initial wavenumbers-1 and -3 MJO

The final case with uniform SST is case U13, shown in Fig. 5. To illustrate which features are nonlinear and which are linear, case U13 is shown in Figs. 5a,b and the linear version of case U13 is shown in Figs. 5c,d. This figure shows that a wavenumber-2 envelope of MJO events arises in both the nonlinear and linear versions, and its existence is due to linear dynamics. Within this envelope, the linear version displays identical MJO events with equal positive and negative amplitudes. On the other hand, the nonlinear dynamics creates a variety of different MJO events with long or short lifetimes, strong or weak amplitudes, stronger positive anomalies than negative anomalies, etc. For instance, in the time period from $t = 150$ to 250 days, there are strong MJOs with positive anomalies above 1 K day^{-1} between $x = 0$ and $10\,000$ km, and, at the same time, there are weaker MJOs with amplitudes below 1 K day^{-1} between $x = 20\,000$ and $30\,000$ km.

4. Nonlinear dynamics with regional variations

While the previous section illustrated nonlinear dynamics with a uniform SST, this section illustrates the effect of an SST with warm-pool regional variations. The variations in the background state $\bar{H}\bar{A}(x) = S^\theta(x)$ are shown in Fig. 6, with a warm pool in the center of the domain from $x \approx 10\,000$ to $30\,000$ km and a cold pool elsewhere.

a. Case WP-MJO: Initial MJO

In case WP-MJO, a warm-pool base state is used with a wavenumber-2 MJO as the initial condition. The long-term evolution of the convective activity is shown in Fig. 7. After an initial adjustment period, the convective activity aligns itself over the warm pool from roughly time $t \approx 2000$ days and thereafter. The MJO events have prominent phases of both active and suppressed convection, and each event has its own individual characteristics in terms of strength, lifetime, regional variations, etc. Furthermore, in addition to the prominent eastward-propagating disturbances, there are instances of localized standing oscillations throughout the domain. For instance, there are standing oscillations localized near $x \approx 11\,000$ km during the period from roughly $t = 2300$ to 2500 days, toward the western end of the warm pool. This is in broad agreement with the visual appearance of standing oscillations in the Indian Ocean, often at the beginning of an MJO event (Lau and Chan 1985; Zhang and Hendon 1997; Kiladis et al. 2005).

To further explore the standing oscillations, the data is projected onto the eastward- and westward-propagating eigenmodes, as shown in Fig. 8. The eigenmode data is obtained by projecting the data vector $[K(x, t), R(x, t), Q(x, t), A(x, t)]^T$ onto the linear eigenmodes in Fourier space, for each wavenumber k and at each time t . The resulting data include the eigenmode anomalies $e_{\text{MJO}}(x, t)$ and $e_{\text{mR}}(x, t)$ of the MJO mode and the moist Rossby mode, respectively; and it should be kept in mind that these linear eigenmodes actually have nonlinear dynamics. The evolution of $e_{\text{MJO}}(x, t)$ and $e_{\text{mR}}(x, t)$ is shown in Figs. 8a,b, respectively, for the final 1600 days from Fig. 7; and the time-averaged root-mean-squares (rms) of the anomalies are shown in Figs. 8c,d, respectively. The MJO mode anomalies are, on average, roughly centered around $x = 20\,000$ km, the location of the maximum SST anomaly. The moist Rossby anomalies have smaller amplitudes than the MJO anomalies; they are not as coherent and their rms is slightly larger in the western part of the warm pool than in the eastern part. This suggests that, in this model, standing oscillations may be slightly more common in the western part of the warm pool than in the eastern part. In some specific instances, standing oscillations from

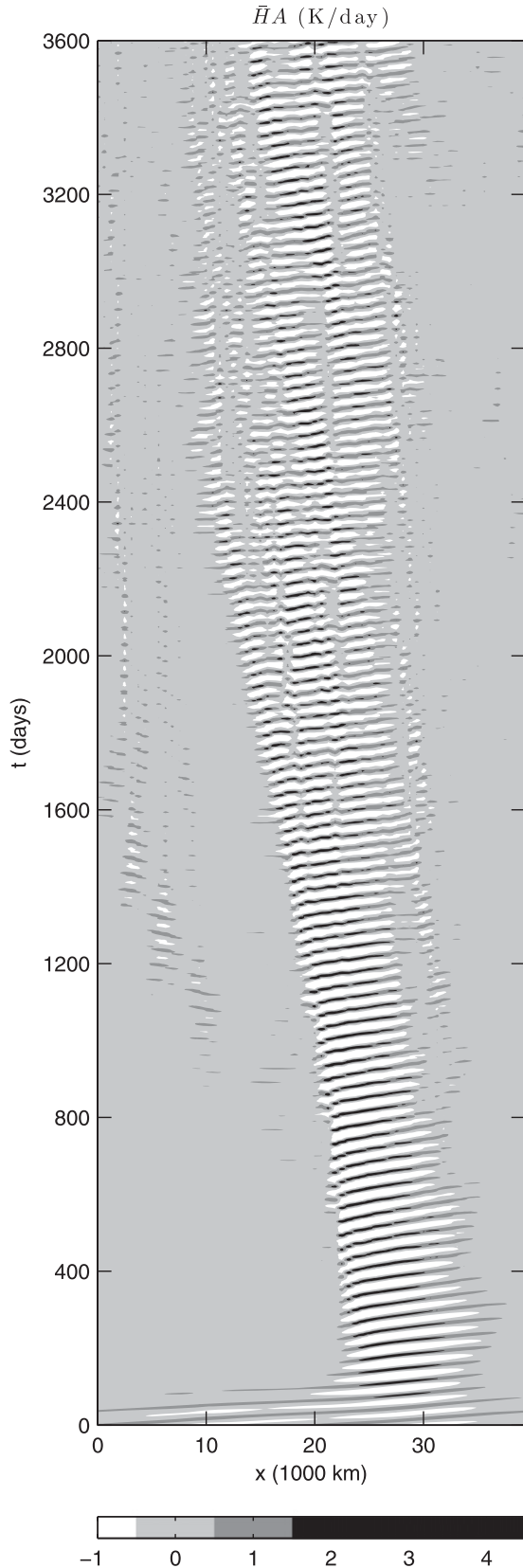


Fig. 7 can be identified in Fig. 8 as instances with anomalies in both e_{MJO} and e_{mR} ; one example is the region localized near $x \approx 11\,000$ km during the period from roughly $t = 2300$ to 2500 days, toward the western end of the warm pool, which was mentioned in the previous paragraph. In the model results here, the visual appearance of standing oscillations—without overwhelming statistical evidence for them—is in accord with the observational analyses of Zhang and Hendon (1997). More instances of visual evidence are shown in the zoomed-in figures described next.

To illustrate the details of a few MJO events, the final 200 days from Fig. 7 are shown in detail in Fig. 9, along with plots of the other variables: $Q(x, t)$, $K(x, t)$, and $R(x, t)$. Two rectangular boxes are drawn in Figs. 9a,b to identify instances of localized standing oscillations: $x = 11\,000$ – $15\,000$ km, $t = 3400$ – 3470 days, and $x = 15\,000$ – $19\,000$ km, $t = 3440$ – 3530 days. Localized standing oscillations are prominent again, later, in the region $x = 15\,000$ – $19\,000$ km, $t = 3550$ – 3600 days (for comparison, no box added). These plots show the details of the significant variations in the MJO events, including their amplitudes, propagation, lifetimes, and/or regional extent.

Moreover, these plots also show significant dry wave activity, which is particularly clear in the plots of K and R in Figs. 9c,d. These plots each display two prominent signals: the MJO signal dominates the warm-pool region in both plots because the MJO includes significant contributions from both K and R structures (cf. Fig. 2), and dry Kelvin and equatorial Rossby waves dominate the cold-pool regions in Figs. 9c,d, respectively. These dry waves can also be seen in the warm-pool region, where they appear as fluctuations in the MJO signal in Figs. 9c,d; and the convergence from these dry waves strongly affects the moisture anomalies, as seen in Fig. 9b; but the signature of the dry waves does not stand out in the convective activity in Fig. 9a, even though they likely contribute to the fluctuations in convective activity indirectly, through the moisture anomalies. It is also interesting that the beginning and end of almost all MJO events appear concomitant with dry wave signals in the cold pool. This appears in four different ways in Figs. 9c,d: (i) Kelvin waves often impinge on the western side of the warm pool near $x \approx 15\,000$ km and appear to “trigger” the next MJO event, (ii) Kelvin waves often appear to be “ejected” into the cold pool when MJO events end near $x \approx 25\,000$ km,

←

FIG. 7. Case WP-MJO: Warm-pool base state with wavenumber-2 MJO as initial condition. Contours of anomalous convective activity $\bar{H}A(x, t)$ for 3600 days.

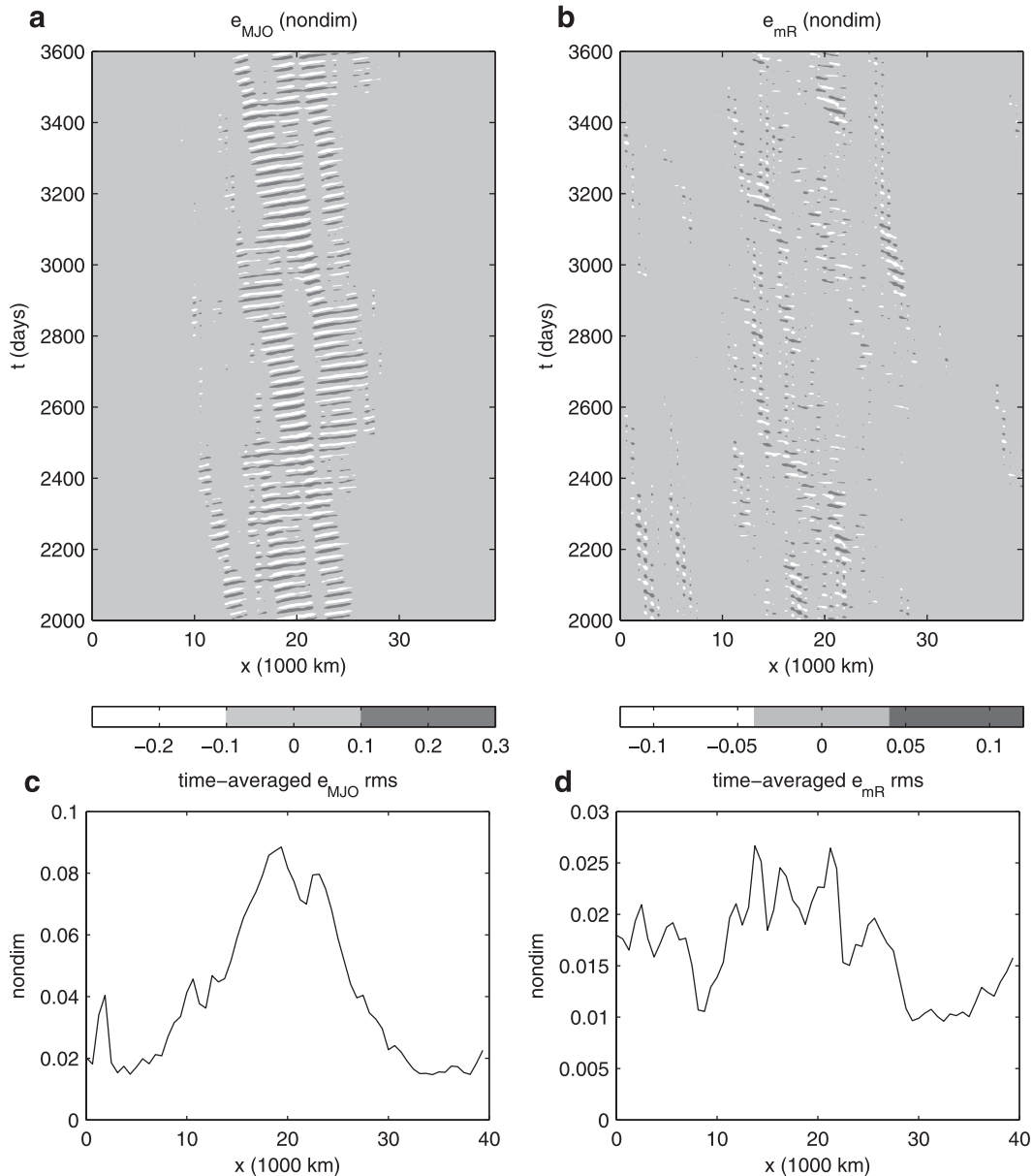


FIG. 8. Case WP-MJO (continued from Fig. 7). Contour plots of data projected onto (a) the MJO eigenmode $e_{\text{MJO}}(x, t)$ and (b) the moist Rossby eigenmode $e_{\text{mR}}(x, t)$, and time averages of the root-mean-square of (c) $e_{\text{MJO}}(x, t)$ and (d) $e_{\text{mR}}(x, t)$.

(iii) equatorial Rossby waves often impinge on the eastern side of the warm pool near $x \approx 25$ 000 km and appear to “terminate” an MJO event, and (iv) equatorial Rossby waves often appear to be ejected into the cold pool when MJO events start near $x \approx 15$ 000 km.

The series of snapshots in Fig. 10 shows the detailed evolution and horizontal structure of an individual MJO event. Four snapshots of $\overline{Ha}(x, y)$, $q(x, y)$, and horizontal velocity are shown at 10-day intervals from $t = 3480$ to 3510 days. The MJO event begins as a localized standing

oscillation between $x \approx 15$ 000 and 20 000 km, as can be seen in Fig. 9 and in the sign changes in \overline{Ha} and q from Figs. 10a,b. The enhanced convection in Fig. 10b is at the center of a horizontal quadrupole vortex structure. Ten days later, the enhanced convection has propagated eastward to $x \approx 22$ 000 km, as shown in Fig. 10c, and it is flanked by significant regions of suppressed convection. Last, the final stage of the life cycle is seen in Fig. 10d, where the enhanced convection has reached the eastern extent of the warm pool near $x \approx 23$ 000–27 000 km, and

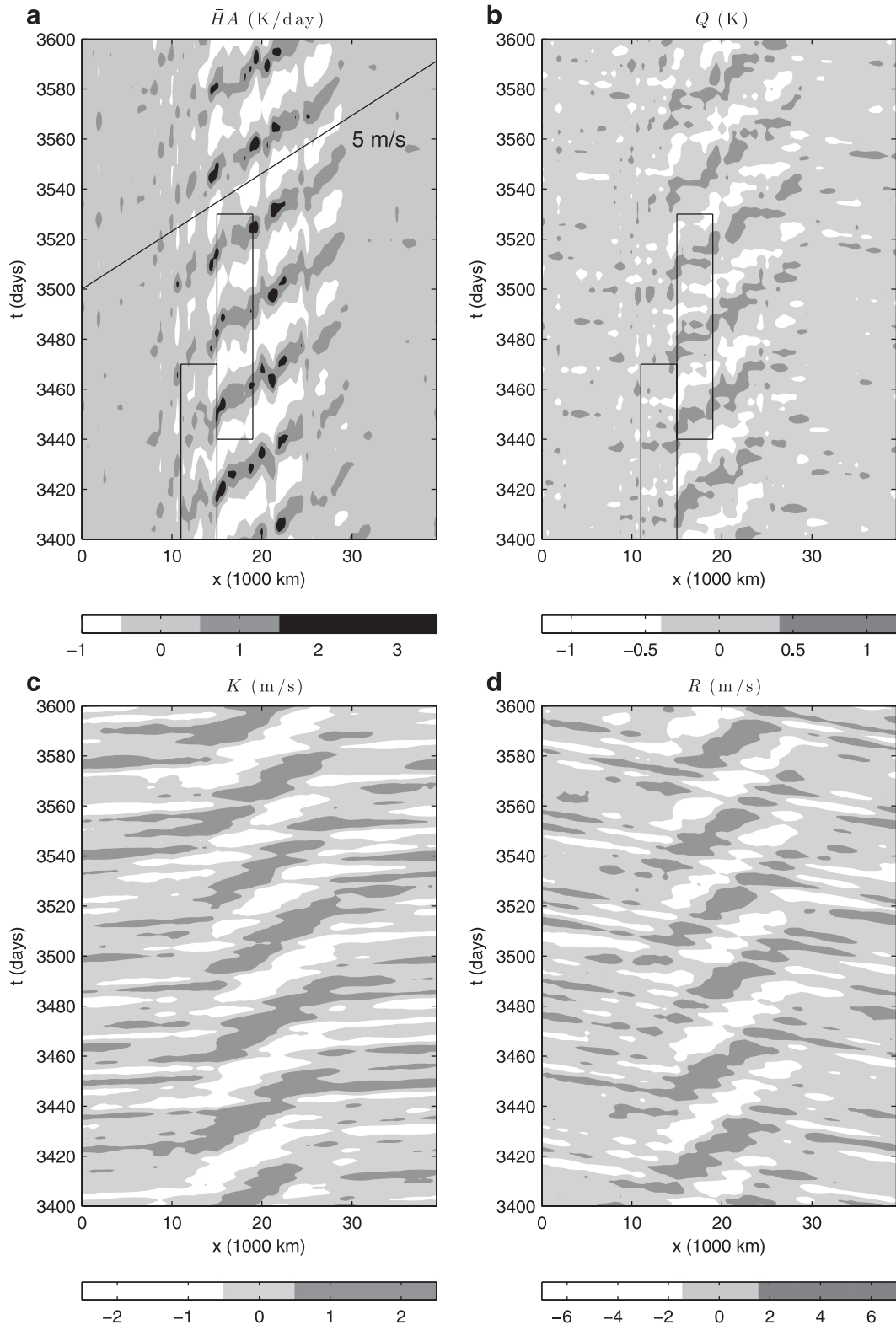


FIG. 9. Case WP-MJO (continued from Fig. 7). Contour plots for the last 200 days from Fig. 7, for times $t = 3400$ – 3600 days: (a) $\bar{H}A(x, t)$, (b) $Q(x, t)$, (c) $K(x, t)$, and (d) $R(x, t)$. Rectangular boxes in (a),(b) show regions of standing oscillations: $x = 11\ 000$ – $15\ 000$ km, $t = 3400$ – 3470 days, and $x = 15\ 000$ – $19\ 000$ km, $t = 3440$ – 3530 days.

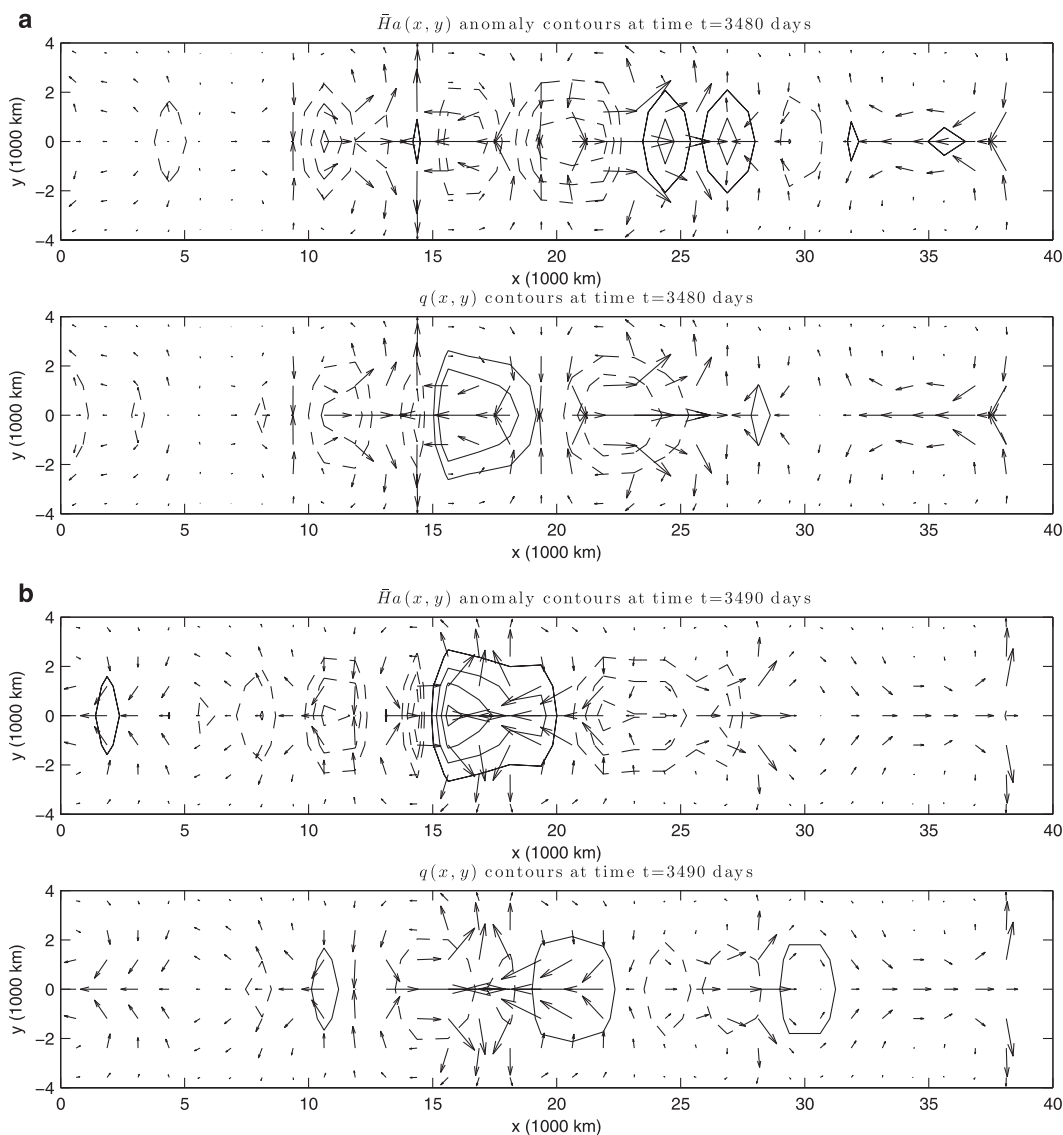


FIG. 10. Case WP-MJO (continued from Fig. 7). Maximum zonal and meridional velocities are (a) 3.25 and 2 m s^{-1} , (b) 3.5 and 1.75 m s^{-1} , (c) 4 and 3 m s^{-1} , and (d) 3.5 and 2.25 m s^{-1} , respectively.

a westerly wind burst is evident [although its strength is weak compared to observations because this model does not include any mechanisms of the MJO's muscle, such as upscale convective momentum transport (Tung and Yanai 2002a,b; Moncrieff 2004; Majda and Biello 2004; Majda and Stechmann 2009a)].

Finally, notice that this nonlinear case demonstrates, to a degree, a rectification of some finer details of the phase relationships in the MJO skeleton, in comparison to linear theory. For instance, in the nonlinear dynamics, the enhanced convection is typically collocated with zonal convergence, as in linear theory; however, there are instances when enhanced convection is collocated with low-level

westerlies, such as the final stages of the life cycle in Fig. 10d, at the eastern extent of the warm pool near $x \approx 24\,000$ km. As another example, in the nonlinear dynamics, enhanced convection is typically led by enhanced lower-tropospheric moisture, as in linear theory; however, there are instances when convection and lower-tropospheric moisture anomalies are collocated, such as the negative anomalies in the eastern part of the warm pool ($x \approx 25\,000$ km) in Fig. 10b and in the western part of the warm pool ($x \approx 17\,000$ km) in Fig. 10c. As mentioned before, even further rectification would be expected to occur from the effects of a refined vertical structure (Lin and Johnson 1996; Myers and Waliser 2003; Kikuchi and

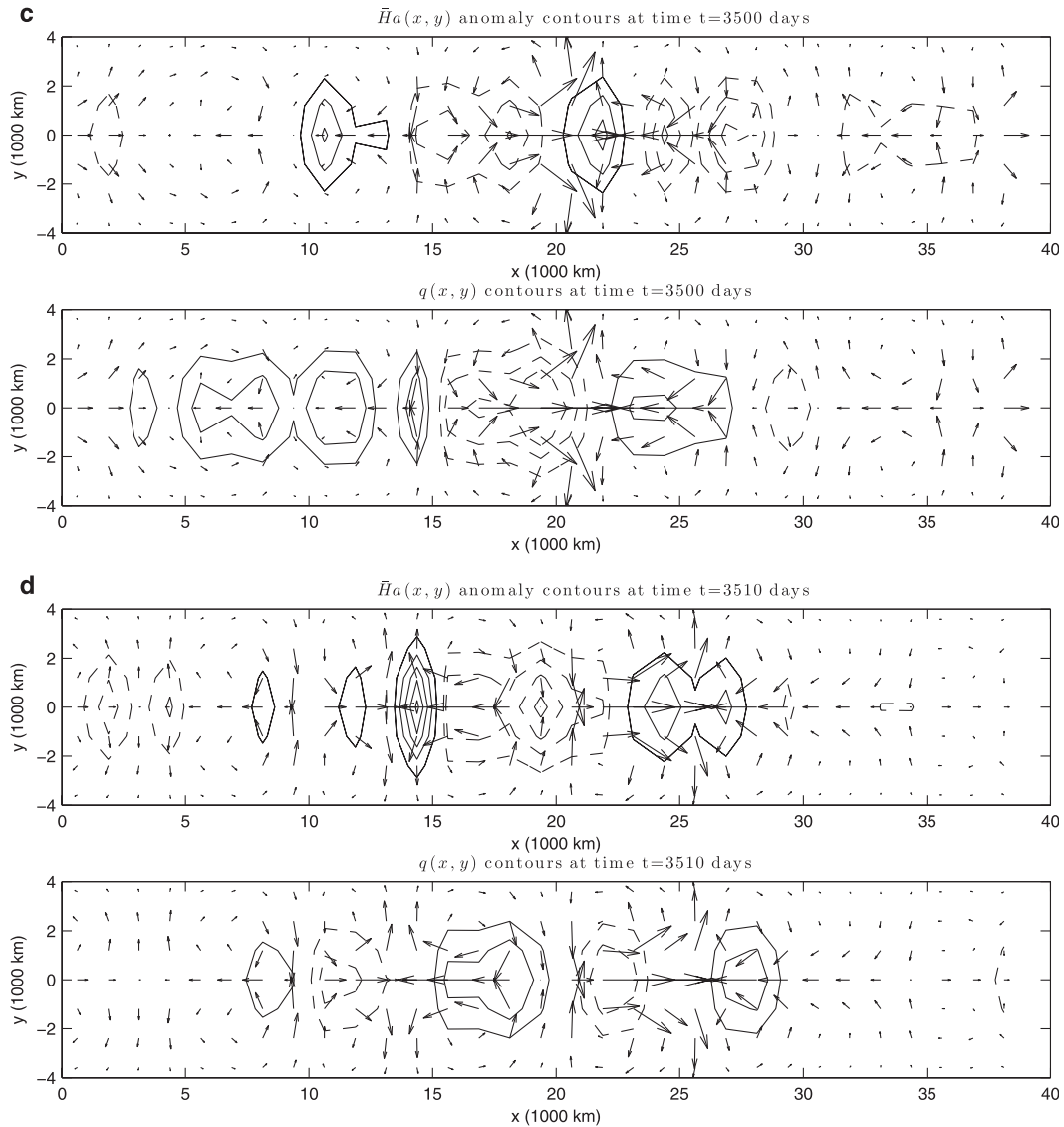


FIG. 10. (Continued)

Takayabu 2004; Kiladis et al. 2005; Tian et al. 2006), upscale momentum transport from mesoscale convective systems and synoptic-scale convectively coupled equatorial waves (Moncrieff and Klinker 1997; Houze et al. 2000; Tung and Yanai 2002a,b; Majda and Biello 2004; Biello and Majda 2005; Majda and Stechmann 2009a), and the effect of land-sea contrasts and surface fluxes (Sobel et al. 2008, 2010). Overall, this case captures the broad fundamental features of the MJO skeleton, in a model with minimal complexity.

b. Case WP-K: Initial Kelvin

Case WP-K is another case with a warm-pool base state, but the initial condition is a wavenumber-2 Kelvin wave. As shown in Fig. 11, both MJO and moist Rossby

modes are excited initially. At later times, from roughly $t = 100$ to 200 days, the central and eastern parts of the warm pool are dominated by the eastward-propagating mode, whereas the far-western warm pool and the cold pool are dominated by the westward-propagating mode (or standing oscillations). This case demonstrates the excitation of the moist waves by an initial dry wave, and it shows, in a nonlinear context, that the eastward-propagating mode is favored in the warm pool over the westward-propagating mode. This latter point corroborates the linear theory results that also suggest that the eastward-propagating mode is more strongly coupled with convection and moisture (Majda and Stechmann 2009b).

c. Case WP-MR: Initial moist Rossby

Finally, Case WP-MR has a warm-pool base state and an initial wavenumber-2 moist Rossby wave (not shown). In this case, the moist Rossby wave does not have its largest amplitudes over the warm pool, as the MJO did (cf. Fig. 7). Instead, the moist Rossby wave has nearly uniform amplitude throughout the domain, with a slightly higher amplitude over the cold pool. This further corroborates the nonlinear Case WP-K and the linear theory results from Majda and Stechmann (2009b) that also suggest that the westward-propagating mode is less strongly coupled with convection and moisture.

5. Conclusions

A minimal, nonlinear oscillator model was presented for the MJO skeleton. As introduced recently by Majda and Stechmann (2009b), the fundamental mechanism of the model involves interactions between (i) planetary-scale, lower-tropospheric moisture anomalies and (ii) the envelope of subplanetary-scale, convection/wave activity. The interactions are neutrally stable (i.e., damping and instabilities on planetary–intraseasonal scales are absent). Furthermore, the model conserves the total energy in (7), which includes a component from the convective activity. The linear and nonlinear waves have been shown to capture, together, the fundamental features 1–3 of the MJO skeleton. Whereas the linear waves were analyzed by Majda and Stechmann (2009b) and summarized here in Fig. 2, the main focus of this paper is the model's nonlinear dynamics. The nonlinear dynamics were studied here in two simple contexts: with a uniform SST (section 3) and with a warm-pool SST (section 4).

With a uniform SST, the model's nonlinear dynamics were studied in the simplest context. For an initial wavenumber-2 MJO, a coherent MJO signal emerged with the fundamental features 1–3 of the MJO skeleton, with both enhanced and suppressed phases of convective activity, and with significant fluctuations of 1–3 K day⁻¹ in the maximum convective activity. Moreover, this nonlinear MJO structure is asymmetric: the enhanced convective region is narrower and has a larger amplitude than the suppressed convection region. Two other cases displayed further nonlinear dynamics of the MJO modes by including multiple MJO wavenumbers initially. These cases showed nonlinear variations in the number, strength, and/or locations of MJO events, such as a strong MJO event followed by a weaker MJO event, similar to TOGA COARE.

With a warm-pool SST, MJO events often began as standing oscillations and then propagated slowly eastward across the warm pool. While displaying the fundamental

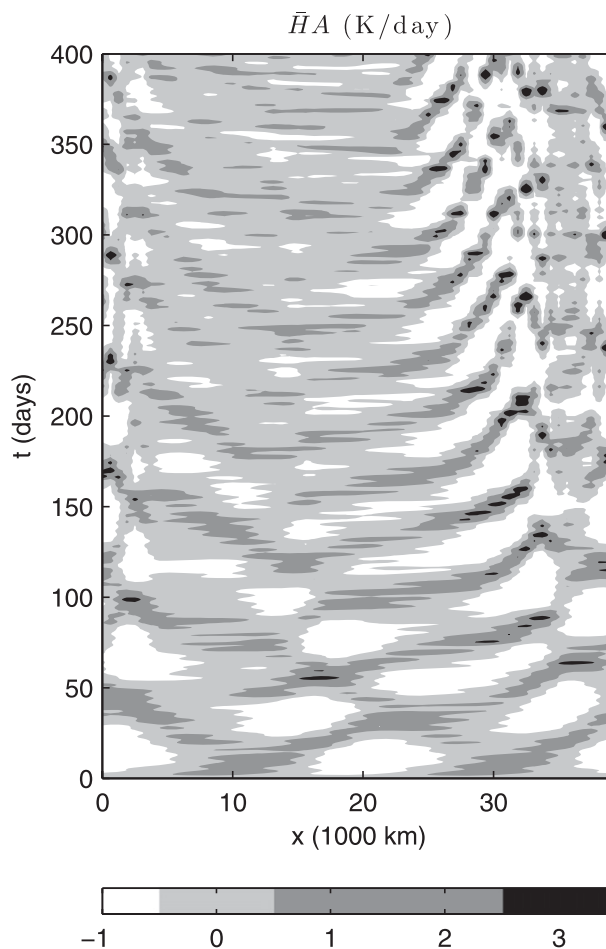


FIG. 11. Case WP-K: Warm-pool base state with initial Kelvin disturbance. Contours of convective activity $\bar{H}A(x,t)$ for 400 days.

features of the MJO skeleton, these MJO events had significant variations in their lifetimes and regional extents, and they displayed intense, irregular fluctuations in their amplitudes. In addition, the MJO events interacted with high-frequency “dry” Kelvin and equatorial Rossby waves, often with these waves appearing to “trigger” or “terminate” an MJO event, and/or with these dry waves appearing to be “ejected” into the cold pool. Furthermore, some details of the phase relationships in the MJO skeleton are rectified to a degree. This was illustrated by instances of collocated anomalies of convective activity and lower-tropospheric moisture and by collocated anomalies of convective activity and westerlies, the latter in resemblance of a westerly wind burst in the final stages of an MJO event. In other cases with a warm-pool SST, an initial dry disturbance excited the low-frequency moist waves, both eastward and westward propagating. The eastward-propagating mode dominated most of the warm pool, whereas the westward-propagating

mode dominated the cold pool and far western parts of the warm pool. As corroboration of the previous linear theory results, the nonlinear moist Rossby mode did not have enhanced amplitude over the warm pool, suggesting that it is not as strongly coupled to moist convective processes as the MJO mode.

While this nonlinear oscillator model is able to capture all of the features of the MJO skeleton summarized above, several finer details of the MJO's "muscle" are not included in this model. These details include, for instance, a refined vertical structure (Lin and Johnson 1996; Myers and Waliser 2003; Kikuchi and Takayabu 2004; Kiladis et al. 2005; Tian et al. 2006); stronger circulation anomalies, such as a westerly wind burst; up-scale momentum transport from mesoscale convective systems and synoptic-scale convectively coupled equatorial waves (Moncrieff and Klinker 1997; Houze et al. 2000; Tung and Yanai 2002a,b; Majda and Biello 2004; Biello and Majda 2005; Majda and Stechmann 2009a); and the effect of land–sea contrasts and surface fluxes (Sobel et al. 2008, 2010). Moreover, the nonlinear oscillator model presented here is a model for only the intraseasonal/planetary-scale features of the MJO. A more complete model should also resolve the detailed subplanetary-scale features within the MJO's envelope of convective activity, including synoptic-scale convectively coupled equatorial waves and/or mesoscale convective systems (Nakazawa 1988; Hendon and Liebmann 1994; Dunkerton and Crum 1995; Yanai et al. 2000; Houze et al. 2000; Masunaga et al. 2006; Kiladis et al. 2009), depending on the model resolution.

Acknowledgments. The authors thank two anonymous reviewers for comments that improved the clarity and presentation of the paper. The research of AJM is partially supported by Grants NSF DMS-0456713, ONR N00014-08-1-0284, and ONR N00014-11-1-0306. SNS was supported by a NOAA Climate and Global Change Postdoctoral Fellowship, a NSF Mathematical Sciences Postdoctoral Research Fellowship, and a start-up grant from the University of Wisconsin—Madison.

APPENDIX

Alternative Model with Weak-Temperature-Gradient Approximation

As mentioned in section 2c, one could create a simplified version of the MJO skeleton model in (2)–(4) by applying the weak-temperature-gradient approximation (Sobel et al. 2001; Majda and Klein 2003). This approximation has both strengths and limitations in this

setting. A nice feature of the approximation is that it leads to a version of the simple (8) exactly:

$$\omega^2 = \Gamma s^\theta (1 - \tilde{Q}). \quad (\text{A1})$$

To see this, the weak-temperature-gradient approximation is applied to the potential temperature equation in (3) to give

$$-u_x - v_y = \bar{H}a', \quad (\text{A2})$$

where $a' = a - \bar{a}$ is the anomaly from the base state $\bar{H}\bar{a} = s^\theta = s^q$. This relation can then be inserted into the q equation in (3) to yield equations for q and a' alone:

$$\begin{aligned} q_t &= -(1 - \tilde{Q})\bar{H}a' \\ a'_t &= \Gamma \bar{a}q, \end{aligned} \quad (\text{A3})$$

where the a equation has been linearized. This is the ordinary differential equation of a simple harmonic oscillator with frequency given by (A1). While the weak-temperature-gradient approximation gives this result in a simple fashion, it also has important limitations. For instance, it is not clear that this weak-temperature-gradient approximation is valid on intraseasonal/planetary scales (Majda and Klein 2003); a valid weak-temperature-gradient approximation is the Seasonal Planetary Equatorial Weak-Temperature-Gradient (SPEWTG) model of Majda and Klein (2003), but it actually appears on somewhat smaller-than-planetary spatial scales and on intraseasonal-to-seasonal time scales. In addition, and more importantly, the dynamics loses its east–west asymmetry; that is, since ω^2 is given by the constant in (A1), both the eastward- and westward-propagating low-frequency modes have the same oscillation frequencies, in contrast to the results in Fig. 2.

REFERENCES

- Austin, J. M., 1948: A note on cumulus growth in a nonsaturated environment. *J. Meteor.*, **5**, 103–107.
- Benedict, J., and D. Randall, 2009: Structure of the Madden–Julian oscillation in the superparameterized CAM. *J. Atmos. Sci.*, **66**, 3277–3296.
- Biello, J. A., and A. J. Majda, 2005: A new multiscale model for the Madden–Julian oscillation. *J. Atmos. Sci.*, **62**, 1694–1721.
- , and —, 2006: Modulating synoptic scale convective activity and boundary layer dissipation in the IPESD models of the Madden–Julian oscillation. *Dyn. Atmos. Oceans*, **42**, 152–215.
- , —, and M. W. Moncrieff, 2007: Meridional momentum flux and superrotation in the multi-scale IPESD MJO model. *J. Atmos. Sci.*, **64**, 1636–1651.
- Bourlioux, A., and A. J. Majda, 1995: Theoretical and numerical structure of unstable detonations. *Philos. Trans. Roy. Soc. London*, **350A**, 29–68.

- Brown, R. G., and C. Zhang, 1997: Variability of midtropospheric moisture and its effect on cloud-top height distribution during TOGA COARE. *J. Atmos. Sci.*, **54**, 2760–2774.
- Chao, W. C., 1987: On the origin of the tropical intraseasonal oscillation. *J. Atmos. Sci.*, **44**, 1940–1949.
- Derbyshire, S., I. Beau, P. Bechtold, J. Grandpeix, J. Piriou, J. Redelsperger, and P. Soares, 2004: Sensitivity of moist convection to environmental humidity. *Quart. J. Roy. Meteor. Soc.*, **130**, 3055–3079.
- Dunkerton, T. J., and F. X. Crum, 1995: Eastward propagating 2–15-day equatorial convection and its relation to the tropical intraseasonal oscillation. *J. Geophys. Res.*, **100** (D12), 25 781–25 790.
- Emanuel, K. A., 1987: An air–sea interaction model of intraseasonal oscillations in the Tropics. *J. Atmos. Sci.*, **44**, 2324–2340.
- Frierson, D. M. W., A. J. Majda, and O. M. Pauluis, 2004: Large scale dynamics of precipitation fronts in the tropical atmosphere: A novel relaxation limit. *Commun. Math. Sci.*, **2** (4), 591–626.
- Gill, A., 1980: Some simple solutions for heat-induced tropical circulation. *Quart. J. Roy. Meteor. Soc.*, **106**, 447–462.
- Grabowski, W. W., 2001: Coupling cloud processes with the large-scale dynamics using the cloud-resolving convection parameterization (CRCP). *J. Atmos. Sci.*, **58**, 978–997.
- , 2003: MJO-like coherent structures: Sensitivity simulations using the cloud-resolving convection parameterization (CRCP). *J. Atmos. Sci.*, **60**, 847–864.
- , and M. W. Moncrieff, 2004: Moisture–convection feedback in the Tropics. *Quart. J. Roy. Meteor. Soc.*, **130**, 3081–3104.
- Hendon, H. H., and B. Liebmann, 1994: Organization of convection within the Madden–Julian oscillation. *J. Geophys. Res.*, **99**, 8073–8084.
- , and M. L. Salby, 1994: The life cycle of the Madden–Julian oscillation. *J. Atmos. Sci.*, **51**, 2225–2237.
- Holloway, C. E., and J. D. Neelin, 2009: Moisture vertical structure, column water vapor, and tropical deep convection. *J. Atmos. Sci.*, **66**, 1665–1683.
- Houze, R. A., Jr., S. S. Chen, D. E. Kingsmill, Y. Serra, and S. E. Yuter, 2000: Convection over the Pacific warm pool in relation to the atmospheric Kelvin–Rossby wave. *J. Atmos. Sci.*, **57**, 3058–3089.
- Khouider, B., and A. J. Majda, 2006: A simple multicloud parameterization for convectively coupled tropical waves. Part I: Linear analysis. *J. Atmos. Sci.*, **63**, 1308–1323.
- , and —, 2007: A simple multicloud parameterization for convectively coupled tropical waves. Part II: Nonlinear simulations. *J. Atmos. Sci.*, **64**, 381–400.
- , and —, 2008a: Equatorial convectively coupled waves in a simple multicloud model. *J. Atmos. Sci.*, **65**, 3376–3397.
- , and —, 2008b: Multicloud models for organized tropical convection: Enhanced congestus heating. *J. Atmos. Sci.*, **65**, 895–914.
- , A. St-Cyr, A. J. Majda, and J. Tribbia, 2011: The MJO and convectively coupled waves in a coarse-resolution GCM with a simple multicloud parameterization. *J. Atmos. Sci.*, **68**, 240–264.
- Kikuchi, K., and Y. N. Takayabu, 2004: The development of organized convection associated with the MJO during TOGA COARE IOP: Trimodal characteristics. *Geophys. Res. Lett.*, **31**, L10101, doi:10.1029/2004GL019601.
- Kiladis, G. N., K. H. Straub, and P. T. Haertel, 2005: Zonal and vertical structure of the Madden–Julian oscillation. *J. Atmos. Sci.*, **62**, 2790–2809.
- , M. C. Wheeler, P. T. Haertel, K. H. Straub, and P. E. Roundy, 2009: Convectively coupled equatorial waves. *Rev. Geophys.*, **47**, RG2003, doi:10.1029/2008RG000266.
- Kim, D., and Coauthors, 2009: Application of MJO simulation diagnostics to climate models. *J. Climate*, **22**, 6413–6436.
- Lau, K. M., and P. H. Chan, 1985: Aspects of the 40–50 day oscillation during the northern winter as inferred from outgoing longwave radiation. *Mon. Wea. Rev.*, **113**, 1889–1909.
- Lau, W. K. M., and D. E. Waliser, Eds., 2005: *Intraseasonal Variability in the Atmosphere–Ocean Climate System*. Springer, 436 pp.
- Lin, J.-L., and Coauthors, 2006: Tropical intraseasonal variability in 14 IPCC AR4 climate models. Part I: Convective signals. *J. Climate*, **19**, 2665–2690.
- Lin, X., and R. H. Johnson, 1996: Kinematic and thermodynamic characteristics of the flow over the western Pacific warm pool during TOGA COARE. *J. Atmos. Sci.*, **53**, 695–715.
- Madden, R. A., and P. R. Julian, 1971: Detection of a 40–50 day oscillation in the zonal wind in the tropical Pacific. *J. Atmos. Sci.*, **28**, 702–708.
- , and —, 1972: Description of global-scale circulation cells in the Tropics with a 40–50 day period. *J. Atmos. Sci.*, **29**, 1109–1123.
- , and —, 1994: Observations of the 40–50-day tropical oscillation—A review. *Mon. Wea. Rev.*, **122**, 814–837.
- Majda, A. J., 2003: *Introduction to PDEs and Waves for the Atmosphere and Ocean*. Vol. 9, *Courant Lecture Notes in Mathematics*, American Mathematical Society, x + 234 pp.
- , and R. Klein, 2003: Systematic multiscale models for the Tropics. *J. Atmos. Sci.*, **60**, 393–408.
- , and J. A. Biello, 2004: A multiscale model for the intraseasonal oscillation. *Proc. Natl. Acad. Sci. USA*, **101**, 4736–4741.
- , and S. N. Stechmann, 2009a: A simple dynamical model with features of convective momentum transport. *J. Atmos. Sci.*, **66**, 373–392.
- , and —, 2009b: The skeleton of tropical intraseasonal oscillations. *Proc. Natl. Acad. Sci. USA*, **106**, 8417–8422.
- , —, and B. Khouider, 2007: Madden–Julian Oscillation analog and intraseasonal variability in a multicloud model above the equator. *Proc. Natl. Acad. Sci. USA*, **104**, 9919–9924.
- Malkus, J. S., 1954: Some results of a trade-cumulus cloud investigation. *J. Meteor.*, **11**, 220–237.
- Maloney, E. D., and D. L. Hartmann, 1998: Frictional moisture convergence in a composite life cycle of the Madden–Julian oscillation. *J. Climate*, **11**, 2387–2403.
- Masunaga, H., T. L’Ecuyer, and C. Kummerow, 2006: The Madden–Julian oscillation recorded in early observations from the Tropical Rainfall Measuring Mission (TRMM). *J. Atmos. Sci.*, **63**, 2777–2794.
- Matsuno, T., 1966: Quasi-geostrophic motions in the equatorial area. *J. Meteor. Soc. Japan*, **44**, 25–43.
- Moncrieff, M. W., 2004: Analytic representation of the large-scale organization of tropical convection. *J. Atmos. Sci.*, **61**, 1521–1538.
- , and E. Klinker, 1997: Organized convective systems in the tropical western Pacific as a process in general circulation models: A TOGA COARE case-study. *Quart. J. Roy. Meteor. Soc.*, **123**, 805–827.
- Myers, D., and D. Waliser, 2003: Three-dimensional water vapor and cloud variations associated with the Madden–Julian oscillation during Northern Hemisphere winter. *J. Climate*, **16**, 929–950.
- Nakazawa, T., 1988: Tropical super clusters within intraseasonal variations over the western Pacific. *J. Meteor. Soc. Japan*, **66**, 823–839.
- Neelin, J. D., I. M. Held, and K. H. Cook, 1987: Evaporation–wind feedback and low-frequency variability in the tropical atmosphere. *J. Atmos. Sci.*, **44**, 2341–2348.

- Raymond, D. J., 2001: A new model of the Madden–Julian oscillation. *J. Atmos. Sci.*, **58**, 2807–2819.
- Roundy, P., and W. Frank, 2004: A climatology of waves in the equatorial region. *J. Atmos. Sci.*, **61**, 2105–2132.
- Salby, M., and H. Hendon, 1994: Intraseasonal behavior of clouds, temperature, and motion in the tropics. *J. Atmos. Sci.*, **51**, 2207–2224.
- , R. R. Garcia, and H. H. Hendon, 1994: Planetary-scale circulations in the presence of climatological and wave-induced heating. *J. Atmos. Sci.*, **51**, 2344–2367.
- Sobel, A. H., J. Nilsson, and L. M. Polvani, 2001: The weak temperature gradient approximation and balanced tropical moisture waves. *J. Atmos. Sci.*, **58**, 3650–3665.
- , E. D. Maloney, G. Bellon, and D. M. Frierson, 2008: The role of surface heat fluxes in tropical intraseasonal oscillations. *Nat. Geosci.*, **1**, 653–657.
- , —, —, and —, 2010: Surface fluxes and tropical intraseasonal variability: A reassessment. *J. Adv. Model. Earth Syst.*, **2** (2), doi:10.3894/JAMES.2010.2.2.
- Thayer-Calder, K., and D. Randall, 2009: The role of convective moistening in the Madden–Julian oscillation. *J. Atmos. Sci.*, **66**, 3297–3312.
- Tian, B., D. Waliser, E. Fetzer, B. Lambrigtsen, Y. Yung, and B. Wang, 2006: Vertical moist thermodynamic structure and spatial–temporal evolution of the MJO in AIRS observations. *J. Atmos. Sci.*, **63**, 2462–2485.
- Tompkins, A. M., 2001: Organization of tropical convection in low vertical wind shears: The role of water vapor. *J. Atmos. Sci.*, **58**, 529–545.
- Tung, W., and M. Yanai, 2002a: Convective momentum transport observed during the TOGA COARE IOP. Part I: General features. *J. Atmos. Sci.*, **59**, 1857–1871.
- , and —, 2002b: Convective momentum transport observed during the TOGA COARE IOP. Part II: Case studies. *J. Atmos. Sci.*, **59**, 2535–2549.
- Waite, M. L., and B. Khouider, 2010: The deepening of tropical convection by congestus preconditioning. *J. Atmos. Sci.*, **67**, 2601–2615.
- Wang, B., and H. Rui, 1990: Dynamics of the coupled moist Kelvin–Rossby wave on an equatorial beta-plane. *J. Atmos. Sci.*, **47**, 397–413.
- Wheeler, M., and G. N. Kiladis, 1999: Convectively coupled equatorial waves: Analysis of clouds and temperature in the wavenumber–frequency domain. *J. Atmos. Sci.*, **56**, 374–399.
- Yanai, M., B. Chen, and W.-W. Tung, 2000: The Madden–Julian oscillation observed during the TOGA COARE IOP: Global view. *J. Atmos. Sci.*, **57**, 2374–2396.
- Zhang, C., 2005: Madden–Julian Oscillation. *Rev. Geophys.*, **43**, RG2003, doi:10.1029/2004RG000158.
- , and H. H. Hendon, 1997: Propagating and standing components of the intraseasonal oscillation in tropical convection. *J. Atmos. Sci.*, **54**, 741–752.